Aerodynamically induced formation of contrails

K. Gierens*, B. Kärcher, H. Mannstein, B. Mayer
DLR Oberpfaffenhofen, Institut für Physik der Atmosphäre, Germany

Keywords: Aerodynamics, Microphysics, Optics, Contrails

ABSTRACT: We study the formation and growth of ice particles induced by the cooling of the air while flowing over the wings of cruising aircraft.

1 INTRODUCTION

Photographs taken in flight show that condensation sometimes starts right above the wings of cruising aircraft. This demonstrates the existence of contrails different from the well studied jet exhaust contrails. Below we present a first investigation of the conditions that lead to the appearance of aerodynamic contrails, along with a characterisation of their basic microphysical and optical properties. Studies of aerodynamic contrails require interdisciplinary research on compressible gas flow over airfoils, ice and aerosol microphysics, and optics of ice crystals, such as outlined here.

2 AERODYNAMICS

As a first step into this new research area, we make simplifying yet sufficiently accurate assumptions that allow us to compute the flow field by straightforward numerical means, circumventing the use of a sophisticated CFD code. As a motivation, we start with a simple back-of-the-envelope calculation.

2.1 *Back-of-the-envelope calculation*

The average pressure difference above minus below the wings is the force that carries the aircraft. Let the aircraft weight be W, its wing area A, then the pressure difference is $\Delta p = -W/A$. For wide body aircraft (e.g. A340, B747) this amounts to a surprisingly large value of typically −50 hPa. Now assume that this pressure difference arises adiabatically in the flow. The corresponding temperature difference is given by $\Delta T / T = [(\kappa-1)/\kappa] (\Delta p / p)$ with $\kappa = c_p/c_V = 1.4$ being the ratio of the specific heats of air. For typical conditions at cruise altitudes (e.g. T = 220 K, p = 220 hPa) we get $\Delta T = -14$ K, i.e. a sudden cooling above the wing that suffices to turn even relatively dry air of, say, $RH_i = 20\%$, into a transient supersaturated state that may allow condensation. This rough calculation suggests that aerodynamically induced condensation should occur at times. The question arises why, on the contrary, it apparently is a rare event. In order to answer this and other questions, we have to perform a more detailed flow calculation.

2.2 *Linearised 2-dimensional flow calculation for compressible flow*

We assume that the flow is adiabatic and circulation free, furthermore that the flow is strictly two-dimensional and stationary. First we define the shape of the airfoil, i.e. the cross section of the wing. We have chosen a simple analytical shape, the Joukowski wing. This already quite realistic wing shape results from a conformal mapping of a unit circle, which is appropriate for our goal (although the Joukowski wing is not used in practice). In particular, it has one sharp (trailing) and one round (leading) edge. If we had an incompressible flow, we could compute the velocity potential and stream functions for the Joukowski wing simply from the corresponding quantities in a flow around a circular cylinder. The analytical form of the latter is known, and applying the same con-

* *Corresponding author:* Klaus Gierens, DLR-Institut für Physik der Atmosphäre, Oberpfaffenhofen, D-82234 Wessling, Germany. Email: Klaus.Gierens@dlr.de

formal mapping to these fields as to the wing shape (i.e. the Joukowski transformation) yields the desired result. However, flow incompressibility requires flow speeds with small Mach numbers, while modern airliners typically cruise at Ma = 0.8. Therefore, we must not assume that the flow is incompressible, and we need another way of computation.

The details of our method will be given elsewhere, here we only present the essential assumptions that lead to the solution. Under the stipulated assumptions, the continuity and Euler equations combine to an equation for the flow potential Φ. We assume that the parallel background flow, (u_∞, v_∞), is perturbed only little by the wing and that the background flow has a small angle of attack relative to the wing. With these assumptions, we may linearise the potential equation. Then perturbations caused by the thickness of the wing and by its camber can be treated separately and are additive, leading to the following ansatz for the potential:

$$\Phi = u_\infty x + v_\infty y + \varphi + \psi, \tag{1}$$

where φ and ψ are the perturbation potentials for wing thickness and camber, respectively. Neglecting perturbation quantities of quadratic and higher order in the equation for the potential then gives:

$$\beta^2 \varphi_{xx} + \varphi_{yy} = 0 \quad \text{and} \quad \beta^2 \psi_{xx} + \psi_{yy} = 0 \text{ with } \beta^2 = 1 - Ma^2 \tag{2}$$

The simple (non-conformal) coordinate transformation $x = \xi$, $\beta y = \eta$, yields the classical Laplace equation for the potentials, for instance $\varphi_{\xi\xi} + \varphi_{\eta\eta} = 0$, which can be solved by various means. We employ the method of singularities, where the perturbation potentials are constructed by suitable superpositions of potentials for singular sources, sinks, and vortices.

From the flow field, we computed a set of trajectories, both below and above the wing, using a 4th-order Runge-Kutta scheme (Press et al., 1989). The perturbation of the (dominating) x-component of the flow speed on the trajectories, $u - u_\infty$, is inserted into a generalised Bernoulli equation to yield the temperatures along the trajectories, viz.

$$T = T_\infty - [(\kappa - 1)/\kappa \, R_a] \, (u^2 - u_\infty^2)/2 \tag{3}$$

where R_a is the specific gas constant of dry air (287 J kg^{-1}K^{-1}). The corresponding pressure is obtained from the Poisson equation, viz.

$$p = p_\infty \, (T / T_\infty)^{\kappa/(\kappa-1)}. \tag{4}$$

Figures 1 and 2a/b show the flow field (streamlines) and the temperature and pressure histories on the trajectories for a case with p_∞ = 350 hPa and T_∞ = 235 K. The wing depth is 11.7 m, wing thickness 1.7 m, and the effective angle of attack is 1°.

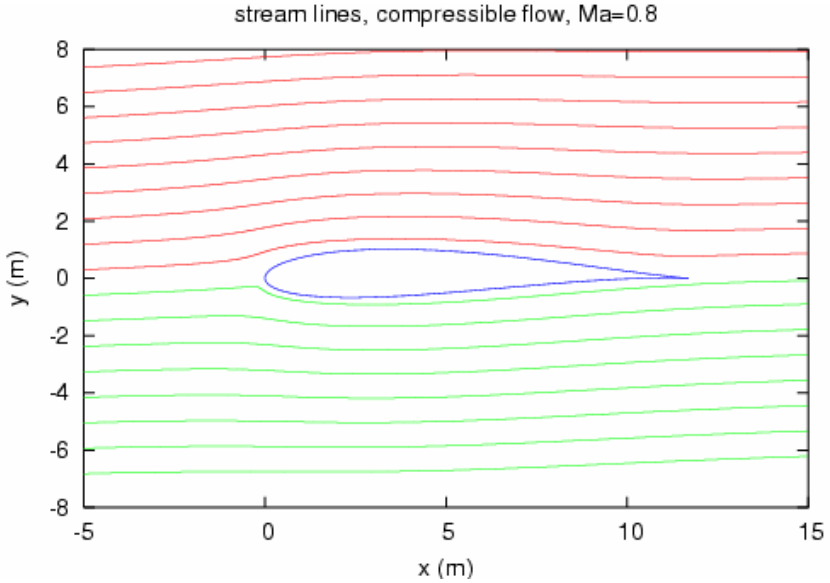

Figure 1. Two-dimensional potential flow field (compressible flow) around a Joukowski airfoil, calculated with the method of singularities. Effective angle of attack: 1°. Mach number: 0.8. The dimensions of the airfoil are typical of a wide-body aircraft close to the fuselage.

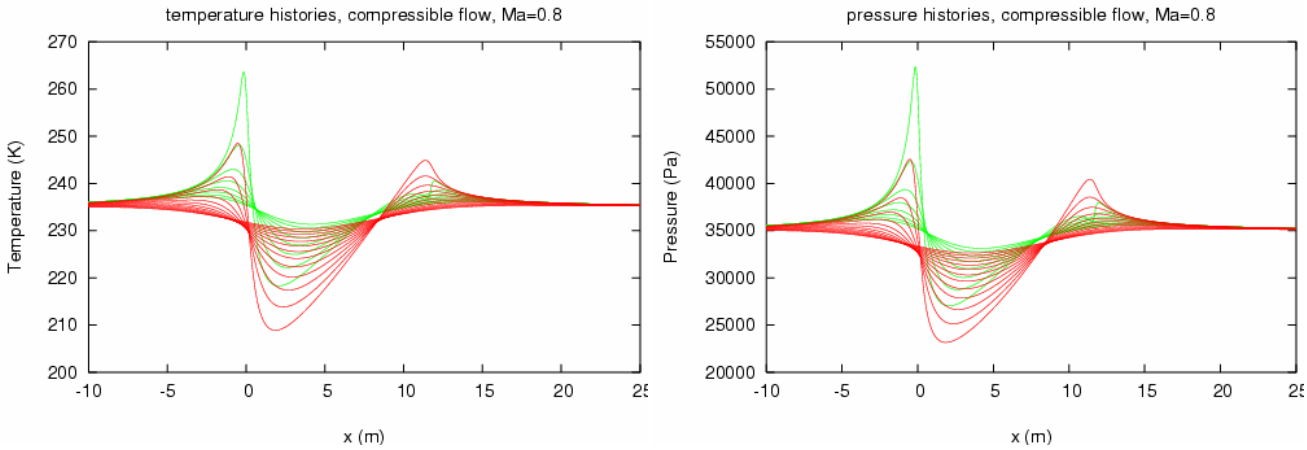

Figure 2. Temperature (left) and pressure (right panel) histories along the streamlines shown in Figure 1.

3 MICROPHYSICS

We employ a comprehensive gas-aerosol-ice trajectory model (Kärcher, 2003) to track the following non-equilibrium processes along one of the T- and p-trajectories close to the wing as shown above. (i) Water condensation on liquid aerosol droplets composed of aqueous H_2SO_4. (ii) Homogeneous freezing of ice from these supercooled aerosol particles. (iii) Depositional growth of the spherical ice particles.

Water uptake on particles is coupled with the gas phase in a strictly mass-conserving manner, so that the evolution of the supersaturation is accurately simulated. A relatively broad lognormal aerosol size distribution has been used for aerosols (mean mass radius 80 nm, geometric standard deviation 1.6, total number concentration 500 cm^{-3}) to cover both Aitken and accumulation mode sizes. Growth of aerosol particles is treated in a Lagrangian manner. This allows us to accurately simulate the water mass fraction in each particle size category to which freezing nucleation rates are extremely sensitive. Growth of ice particles is treated with a moving centre size structure that is virtually free of numerical diffusion. We prescribe an ambient ice supersaturation of RH_i = 140% just below the homogeneous freezing threshold and an H_2O deposition coefficient of unity to maximize ice particle growth. We use a time step of 1 µs for these simulations.

Figure 3 shows results of the microphysical calculations. The legend denotes times and corresponding distances behind the leading wing edge. The ice crystal size distributions (solid curves) are generated from homogeneous freezing of liquid aerosol droplets (dashed). Nucleation is finished as the air parcel moves across the wing (after ~16 m). In the subsequent growth phase in the highly supersaturated air, mean ice particle radii increase to ~2.8 µm after ~680 m.

Note that the ice particle spectrum becomes essentially monodisperse shortly after nucleation. Laminar flow and monodispersity are the key prerequisites for the colourful appearance of aerodynamic contrails, as studied in Section 4. Jet exhaust contrails, on the contrary, appear white because plume turbulence quickly mixes contrail ice particles with slightly different sizes and thus broadens their size spectrum.

Interestingly, the smallest droplets freeze first, followed by freezing of larger droplets, until practically all available aerosol particles are depleted. At first glance, this seems to contradict the common notion that larger particles freeze first owing to their larger volume. However, this assumes that aerosol particles are in equilibrium with ambient H_2O, regardless of size. During the formation of aerodynamic contrails, RH_i changes dramatically on the time scale of ~10 µs. This is of the same order as the composition change time scale dictated by diffusion of H_2O molecules in air. For the small aerosol particles, the latter time scale is proportional to particle surface area. This implies that they adjust faster to increasing RH_i and become water-rich much faster than larger particles, and hence freeze earlier despite a smaller volume. The fact that the time scale for a change in radius is somewhat longer than the time scale for freezing explains why the ice particles start to grow significantly only after nucleation is shut off. It is possible that more and slightly smaller ice

particles would form if we prescribed a larger concentration of aerosol particles. These and other aspects will be addressed in more detail in future work by means of sensitivity studies.

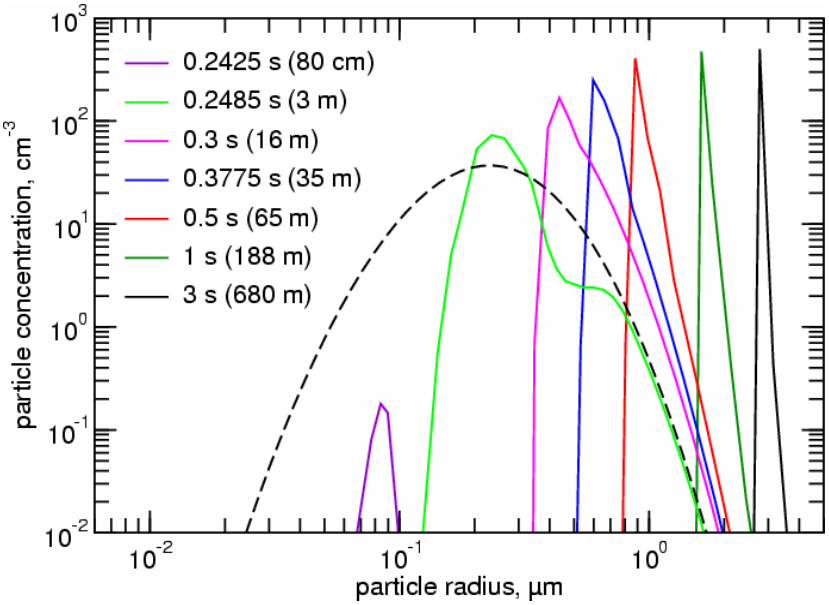

Figure 3. Ice crystal size distributions for various distances (times) behind the leading edge of the wing along the trajectory closest to and above the wing.

4 RADIATION

To determine the colour of the contrail, the scattering coefficient was calculated from the size distributions in Figure 3 using the theory by Mie [1908] for spherical ice particles. The well-known Mie code by Wiscombe [1979] as provided by the libRadtran radiative transfer package [Mayer and Kylling, 2005] was used for this purpose.

Figure 4a shows the extinction efficiency at 550 nm (solid line) as function of the particle radius. The typical features of a monodisperse particle distribution are clearly visible: the Rayleigh limit for particles much smaller than the wavelength, where the extinction efficiency increases rapidly with particle size; and the geometrical optics limit for particles much larger than the wavelength, where the extinction efficiency approaches 2 (that is, the extinction cross section is twice the geometrical cross section). In the size range where the particle radius is comparable to the wavelength, the extinction efficiency shows characteristic oscillations and reaches its maximum where the radius equals the wavelength of the radiation. In the visible spectral range, absorption is negligible and the scattering efficiency equals the extinction efficiency.

From these considerations we may immediately conclude that the scattering coefficient of a monodisperse particle distribution strongly depends on wavelength; if illuminated with white light, selective scattering of colours will cause the scattered radiation to be coloured: e.g., crystals with 400 nm radius will scatter blue most efficiently and the scattered radiation will appear blue; crystals with 700 nm will appear red as the maximum of the scattering cross section occurs at 700 nm. For a polydisperse size distribution, these effects are reduced, and if the size distribution is too wide, they will vanish completely. Hence the appearance of colours indicates a narrow size distribution.

To calculate the actual colour of the contrail, a full radiative transfer calculation is required in principle, to calculate spectral radiance. However, since the optical thickness is small we used a very simple single-scattering approximation: the scattered radiance is assumed to be proportional to the incident (extra-terrestrial) irradiance times the scattering coefficient. This calculated spectral irradiance is converted to colours using “specrend” by John Walker, available at http://www.fourmilab.ch/documents/specrend/. Spectral radiance is converted to X, Y, and Z using the respective CIE colour matching functions, which are then converted to device-dependent colour-coordinates R, G, and B with the respective EBU matrix.

Figure 4a shows the calculated colours as a function of ice particle radius for a monodisperse size distribution. As outlined above, colours are most pronounced in the size range where the change of the extinction efficiency with wavelength is strongest. Figure 4b, finally, shows the colours to be expected for the size distributions from Figure 3. Size distributions were provided every 0.001 seconds from 0.24 seconds to 6 seconds. Extinction efficiencies were calculated with Mie theory and integrated over the size distribution to get the spectral extinction coefficient, multiplied with the spectral extraterrestrial irradiance, and converted to colours. Figure 4b shows the effective ice particle radius. The colours nicely match the colours in the photograph, indicating that growth with time as well as the width of the size distribution were realistic.

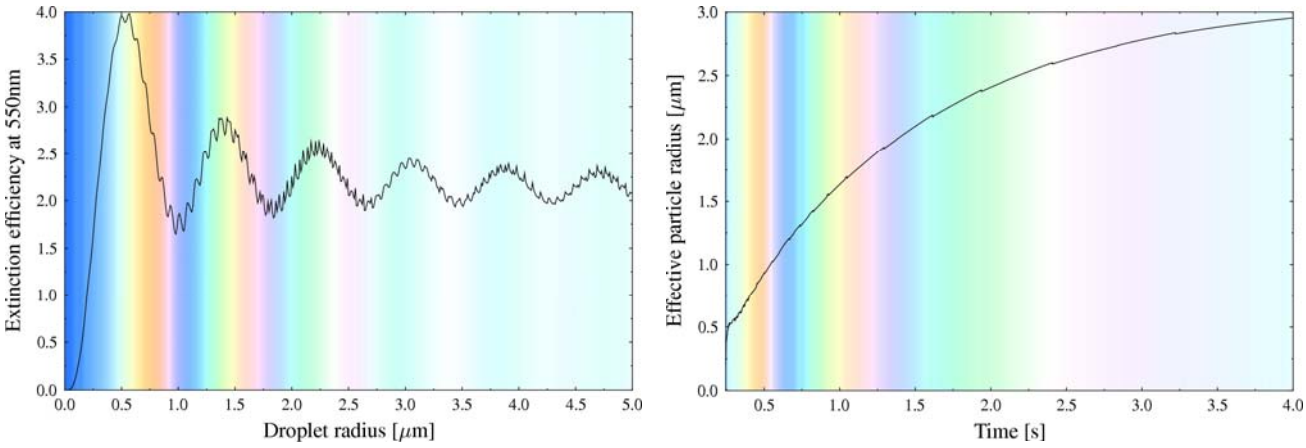

Figure 4. (a) Extinction efficiency for a monodisperse ice particle distribution and colour of the scattered radiation in single-scattering approximation; (b) effective radius and colour for the size distributions from Figure 3 as a function of time.

5 EXAMPLE

On 12 June 2005 from 14:59 to 15:06 Bejing time (~07:00 UTC), pilot and photographer Jeff Well took a series of photos of an exceptionally colourful iridescent contrail produced by an A340-313X aircraft in 9600 m altitude, just 1200 m above his position on the same route over eastern China. Both aircraft were heading to North-West (329°) from 32° 14.8' N, 119° 46.7' E to 32° 56.8' N, 119° 10.1' E. From NCEP reanalysis data we estimate a temperature of –40°C, the aircraft altitude is very close to the 300 hPa pressure level.

The series of photos displayed in Figure 5 shows the development of contrails that cannot be explained by the Schmidt-Appleman criterion. Jet contrails produced from the mixing of exhaust gases with the ambient air would show up as 4 separate lines behind the engines and start later. The onset of the aerodynamic contrails occurs directly above the wings and is stronger close to the body of the aircraft. Thin vortex lines originate from the wing tips and get mixed into the wake vortices.

6 CONCLUSIONS AND OUTLOOK

Photographs demonstrate that aerodynamic contrails occur preferentially above the inner parts of the wings, where the uplift is largest. Hence, aerodynamic contrails may become more relevant for a potential future fleet of blended wing-body aircraft with significantly larger wing depths.

Future work will study the properties of the numerous small ice crystals produced in the adiabatic air flow over wings of airliners, the impact of ambient conditions and background aerosol properties on early aerodynamic contrail formation and evolution, and how common this process occurs relative to jet exhaust contrails that form according to the Schmidt-Appleman theory.

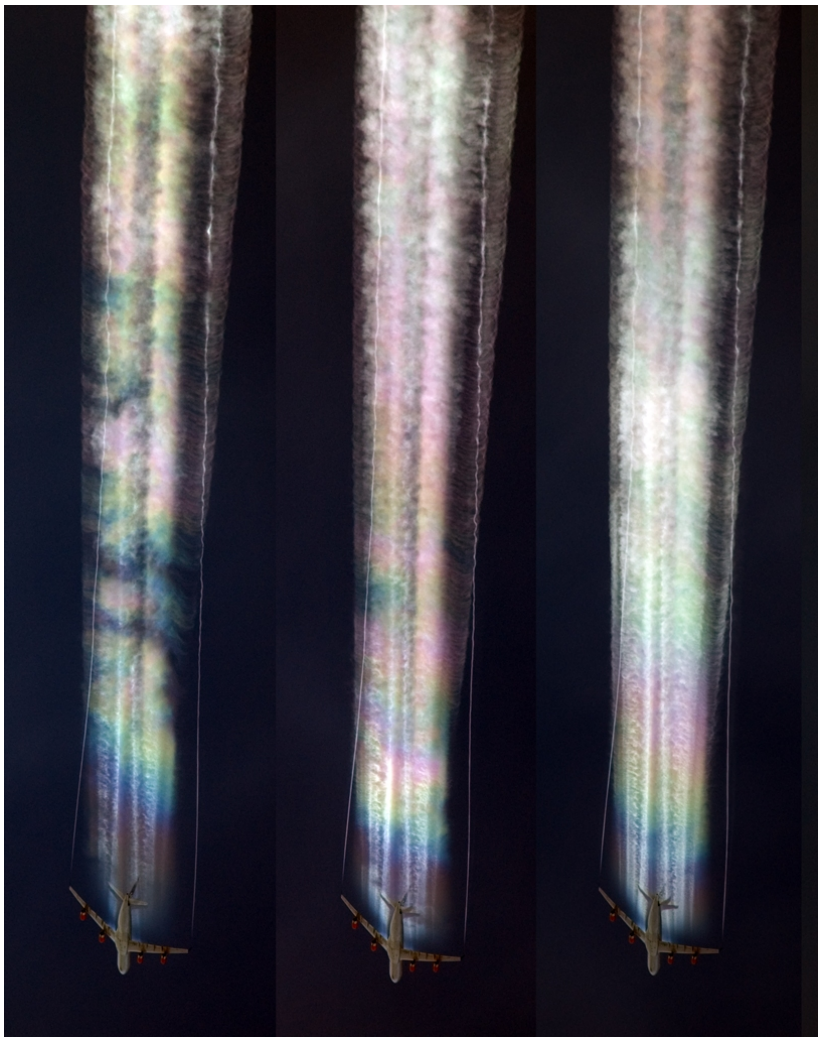

Figure 5. Series of photographs of an aerodynamically induced contrail. Note the iridescent colours. The formation and colourful appearance of such contrails are explained by the combination of aerodynamical, microphysical, and radiative processes outlined in this paper.

ACKNOWLEDGEMENT

The photographs shown here are all taken by pilot Jeff Well. We thank Jeff Well for allowing us to use his photographs of aerodynamic contrails. Many other photographs of aerodynamic contrails can be found on www.airliners.net. This work is supported by the DLR/HGF project Particles and Cirrus Clouds (PAZI-2).

REFERENCES

Kärcher, B., 2003: Simulating gas-aerosol-cirrus interactions: Process-oriented microphysical model and applications. *Atmos. Chem. Phys, 3,* 1645–1664.

Mayer, B., and A. Kylling, 2005: Technical Note: The libRadtran software package for radiative transfer calculations: Description and examples of use. *Atmos. Chem. Phys., 5,*1855–1877.

Mie, G., 1908: Beitraege zur Optik trueber Medien, speziell kolloidaler Metalloesungen. *Annalen der Physik*, Vierte Folge, 25(3):377–445.

Press, W.H., B.P. Flannery, S.A. Teukolsky, and W.T. Vetterling, 1989: *Numerical Recipes.* Cambridge University Press, Cambridge, UK, ISBN 0 521 38330, 702 pp.

Wiscombe, W.J., 1996: Mie Scattering Calculations: Advances in Technique and Fast, Vector-Speed Computer Codes. Technical Report TN-140+STR, NCAR, 1979, edited and revised 1996.